

# Design rule for industrial scale sintering of $UB_4$ – $UBC$ composites with high uranium density

Riley Moeykens<sup>1, 2</sup>, Anthony Albert-Harrup<sup>1, 2</sup>, David Simonne<sup>1, 2</sup>, Mehmet Topsakal<sup>3</sup>, and Ericmoore Jossou<sup>\*1, 4</sup>

<sup>1</sup>Materials in Extreme Environments Laboratory, Massachusetts Institute of Technology, 77 Massachusetts Ave, Cambridge, 02139, MA, USA

<sup>2</sup>Department of Nuclear Science and Engineering, Massachusetts Institute of Technology, 77 Massachusetts Ave, Cambridge, 02139, Massachusetts, United States

<sup>3</sup>Department of Nuclear Science and Technology, Brookhaven National Laboratory, Upton, 11973, New York, United States

<sup>4</sup>Electrical Engineering and Computer Science, Massachusetts Institute of Technology, 77 Massachusetts Ave, Cambridge, 02139, Massachusetts, United States

6th March 2026

## Abstract

Uranium borides are promising candidate fuel forms for use in advanced nuclear reactors due to their high thermal conductivity and potential for dual use as both fuel and burnable absorber. In this work, uranium tetraboride ( $UB_4$ ) and uranium monoborocarbide ( $UBC$ ) composite were synthesized by using industrially scalable borocarbothermic reduction method. The high temperature structural evolution of as-synthesized borides was investigated using *in situ* synchrotron X-ray diffraction (SXR). The oxidation behavior was further characterized using a combination of SXR and thermogravimetric analysis (TGA), allowing direct comparison with other potential accident tolerant fuels such as  $UB_2$ ,  $U_3Si_2$ , UC and UN. The  $UB_4$ – $UBC$  shows higher uranium loading than monolithic  $UB_4$  and demonstrates promising oxidation behavior at high temperature, pointing to its potential as an improved uranium boride-based fuel form.

**Keywords**— Diffraction, Uranium, Fuels, Borides, ATF

## 1 Introduction

In 2011, the severe accident at Fukushima Daiichi Power Station pointed to the limitations of the conventional uranium dioxide-zirconium fuel-cladding system under severe accident scenarios. This event motivated renewed research into advanced fuel concepts leading to international efforts in the development of accident tolerant fuels (ATFs). The U.S. Congress and the Department of Energy’s Office of Nuclear Energy launched the ATF program with the objective of developing non-traditional fuel and cladding systems that can withstand accident scenarios, such as loss-of-coolant events over extended period of time usually ( $>1$ h)[8]. Such fuels must show improved performance during normal operations, transients, design-basis and beyond design-basis accidents, as well as compatibility with non-traditional coolant and varied neutron-spectra.

Many of the proposed long-term ATF concepts, such as  $UB_2$ , UC, UN and  $U_3Si_2$  fuels, have performance, and safety advantages over  $UO_2$  such as improved thermal conductivity and higher fissile density[16, 13, 22, 19]. However, there is limited understanding of their thermophysical properties, pellet-cladding chemical and mechanical interactions, and irradiation behavior. With recent improvements in advanced computing[10, 34], throughput irradiation facilities[4], and advanced characterization tools, such as synchrotron-based X-ray scattering and spectroscopy techniques[9, 24, 35], the acceleration in qualification of ATFs is now more feasible than ever.

In particular, uranium borides are of interest as ATFs for use in light water reactors (LWRs) and high temperature gas reactors (HGTRs). These materials are high-temperature refractory metalloids with a high thermal conductivity, improved thermal stability[23], and with potential for

---

\*Corresponding author, ejossou@mit.edu

use as a burnable absorber[22] or as a composite with  $\text{UO}_2$  or  $\text{U}_3\text{Si}_2$ [19, 39, 40, 10]. The high thermal conductivity reduces the center-line fuel temperature, enhancing tolerance to operational transients and loss-of-coolant accident conditions. Previous work has reported an oxidation onset temperature as high as  $500^\circ\text{C}$  for  $\text{UB}_4$ [14]. However, a comprehensive understanding of the oxidation behavior of uranium borides is limited. Although  $\text{UB}_2$  and  $\text{UB}_4$  appear to have improved thermophysical properties for use as nuclear fuels, the high temperature structural stability, oxidation behavior and irradiation behavior at temperatures and conditions relevant to accident scenarios are not well known. While  $\text{UB}_2$  has improved uranium loading compared to  $\text{UO}_2$ , the sintering temperature is demonstrated to be as high as  $1800^\circ\text{C}$  based on recent studies[38]. Meanwhile,  $\text{UB}_4$  and uranium monoborocarbide (UBC) can be sintered at substantially lower temperatures, making them attractive alternatives from a manufacturing perspective, particularly if comparable thermophysical performance can be achieved with reduced processing energy.

$\text{UB}_4$  has a tetragonal phase which is isomorphous with other tetraborides such as  $\text{ThB}_4$  and  $\text{CeB}_4$ [7] and belongs to the  $P4/mbm$  space group[41]. The  $\text{UB}_4$  phase forms over a boron concentration range of  $\approx 74\text{at}\%$  to  $85\text{at}\%$ , with stoichiometric compositions near  $85\text{at}\%$  boron producing a pure  $\text{UB}_4$  phase[7]. The reported linear coefficient of thermal expansion (CTE) is  $7.1 \times 10^{-6} \text{K}^{-1}$  over the temperature range  $295 \text{K}$  to  $1275 \text{K}$ [27], while a more recent measurement indicates a CTE of  $8.7 \times 10^{-6} \text{K}^{-1}$  at  $400 \text{K}$ [22]. Although  $\text{UB}_4$  demonstrates favorable thermomechanical properties, its uranium density of ( $7.94 \text{g/cm}^3$ )[28] is lower than that of  $\text{UO}_2$  ( $9.67 \text{g/cm}^3$ )[7]. In comparison, UBC has a higher uranium loading ( $\approx 10.9 \text{g/cm}^3$ ), suggesting that  $\text{UB}_4$ -UBC composites could achieve uranium densities similar to  $\text{UO}_2$  while maintaining the beneficial characteristics of uranium borides.

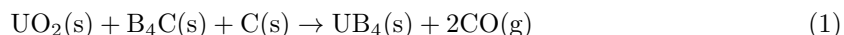
The UBC ternary system has been investigated as early as the 1980s due to interesting magnetic properties, and potential as a standalone nuclear fuel[32]. The UBC crystal structure belongs to the  $Cmcm$  space group, with an orthorhombic structure[32] whereby  $a$  is  $3.5927 \text{\AA}$ ,  $b$  is  $11.9889 \text{\AA}$ , and  $c$  is  $3.3474 \text{\AA}$ [30]. Early works focused mainly on resolving the crystallography and thermal stability of UBC and higher order UBC alloys[32, 31, 30, 2]. However, the high temperature thermal stability and oxidation behavior is not well known or lacking. The melting point of UBC has been determined to be  $2144(25)^\circ\text{C}$ [32]. While this temperature is high, it is lower than the melting temperature of  $\text{UB}_4$  which is  $\approx 2500^\circ\text{C}$ [28]. Meanwhile,  $\text{UO}_2$  has a melting point of  $2840(20)^\circ\text{C}$ [25] with well-known oxidation products such as  $\text{UO}_3$  and  $\text{U}_3\text{O}_8$  at elevated temperatures. Furthermore, there are not many documented studies investigating the air oxidation behavior of UBC. It has generally been observed that while actinoid metal borocarbides have high oxidation resistance in dry air, they rapidly hydrolyze in moisture[30]. Therefore, we hypothesize that the formation of a  $\text{UB}_4$ -UBC composite will improve the oxidation resistance while also increasing uranium loading.

Uranium borides have been fabricated by arc melting[22, 38, 21, 14], suitable for research purpose due to the small batch processing. Meanwhile the borocarbothermic reduction reaction approach is industrially scalable but requires the optimization of several parameters such as sintering temperature, time and environments. Turner *et al.* recently fabricated  $\text{UB}_2$  based on borocarbothermic reduction at  $1800^\circ\text{C}$  for 1 h[38], while the synthesis of  $\text{UB}_4$  has been demonstrated by the same method at  $1500^\circ\text{C}$  in a flowing argon environment[14]. The sintering of a  $\text{UB}_4$ -UBC is expected to occur at relatively lower sintering temperature compared to  $\text{UB}_2$  but with comparable uranium loading and improved oxidation behavior. Therefore, in this work we systematically optimized carbocarbothermic solid state sintering method to fabricate  $\text{UB}_4$  and  $\text{UB}_4$ -UBC composites, as well as investigate the structural and oxidation behavior using scanning electron microscope (SEM), energy dispersive X-ray (EDX) imaging, *in situ* high temperature synchrotron X-ray diffraction (SXRD) measurements, and thermal gravimetric analysis (TGA).

## 2 Methodology

### 2.1 Fuel Sintering

The synthesis of  $\text{UB}_4$  proceeded via the following reaction[14]:



The initial feedstocks consisted of  $\text{UO}_2$  (95% purity,  $1 \mu\text{m}$  to  $3 \mu\text{m}$  particle size),  $\text{B}_4\text{C}$  (99.99% purity,  $45 \mu\text{m}$ , and graphite (99.99%,  $297 \mu\text{m}$ ). Powder handling was performed in a double-sided UNILab Pro MBraun glovebox under high-purity argon (99.99%), with oxygen and moisture levels maintained below 0.5 ppm. To ensure powder homogeneity prior to sintering, the powders were ball-milled in a tungsten carbide jar with stainless steel balls at rotational speeds of 300 rpm to 400 rpm. The milled powders were subsequently uniaxially pressed into pellets under a load of 10000 lbs for 1 min to 2 min. The resulting green pellets had masses of approximately 0.5 g to 2 g,

and thicknesses of several millimeters.

The samples were sintered in an alumina-tube furnace under flowing argon at  $\approx 100$  sccm (Standard Cubic Centimeters per Minute) at temperatures up to  $1700^\circ\text{C}$ . The furnace temperature was increased at a rate of  $5^\circ\text{C min}^{-1}$ , with 30 min isothermal holds at  $500^\circ\text{C}$  intervals.  $\text{UB}_4$  specimens were sintered in alumina crucibles, whereas  $\text{UB}_4\text{-UBC}$  specimens were sintered in graphite crucibles to provide excess carbon and thereby promote UBC formation during sintering.

## 2.2 Oxidation Experiments

Oxidation experiments were conducted by following two different routes at temperatures ranging from room temperature to  $900^\circ\text{C}$ : (I) pre-air oxidation in a tube furnace for *ex situ* and *in situ* SXR analysis and (II) thermogravimetric analysis of weight change due to oxidation in synthetic air (21.49 %  $\text{O}_2$  in  $\text{N}_2$ ). For SXR characterization, small quantities of the sample, either in the form of a coarse powder or as a small piece of a sintered pellet with a mass on the order of tens of milligrams, were placed into small alumina crucibles which were then placed inside a larger alumina crucible positioned at the center of the furnace. The  $\text{UB}_4$  samples were oxidized in flowing compressed air at flow rate of  $\approx 100$  sccm at  $350^\circ\text{C}$  and  $900^\circ\text{C}$  while the  $\text{UB}_4\text{-UBC}$  samples were oxidized in moist air under laboratory ambient conditions, where exposure to atmospheric humidity was unavoidable, at temperatures of  $300^\circ\text{C}$  and  $900^\circ\text{C}$ .

Thermogravimetric analysis (TGA) was performed using a TA Instruments Discovery TGA 5500 at the MIT Institute for Soldier Nanotechnologies (ISN). The instrument operates over a temperature range of  $40^\circ\text{C}$  to  $1000^\circ\text{C}$  with a temperature precision of  $\pm 0.005^\circ\text{C}$  and a mass resolution of  $0.1\ \mu\text{g}$ . Oxidation behavior was evaluated under flowing synthetic air at  $25\ \text{mL min}^{-1}$  using a temperature program consisting of an equilibration at  $50^\circ\text{C}$  followed by a linear ramp of  $5^\circ\text{C/min}$  to  $900^\circ\text{C}$ . High-purity alumina crucibles (6.8 mm outer diameter, 4 mm height,  $\approx 300$  mg; MSE Supplies) were first subjected to the same thermal and gas flow conditions to establish a baseline and account for background mass changes. Subsequently, 2 mg to 3 mg of uranium boride powder was loaded into the crucibles for thermal analysis. Baseline correction was performed by applying a spline fit to the empty-crucible data and subtracting this background from the sample measurements over the entire temperature range, enabling accurate determination of oxidation-induced mass changes.

## 2.3 SEM imaging

SEM and EDS images were collected to determine the microstructure, the elemental composition, and homogeneity after sintering. The Zeiss Sigma 300 VP Field Emission SEM located at the MIT ISN was used for imaging. A voltage of 25 kV was used for the EDS data collection, to ensure that the electron energy was well above the uranium L-a edge at 13.6 keV.

## 2.4 Synchrotron X-ray diffraction measurement and analysis

XRD measurement experiments were conducted at the 28-ID-2 beamline located at the National Synchrotron Light Source-II (NSLS II) at Brookhaven National Laboratory (BNL). The oxidation conditions, sample preparation, and heating profile during measurement at the 28-ID-2 beamline varied between the  $\text{UB}_4$  and  $\text{UB}_4\text{-UBC}$  samples. The differing heating profiles are illustrated in Figure 1a.

In preparation for the XRD measurements at the 28-ID-2 beamline at NSLS II, powder samples were loaded into quartz capillaries to meet the beamline radiological containment requirements. Due to the radioactive nature of the sample, all samples were doubly contained using two concentric quartz capillaries to mitigate the risk of contamination in the event of breakage during the experiments as shown in Figure 1b.

The dimensions of the quartz capillaries and sealants varied slightly between experiments. For the  $\text{UB}_4\text{-UBC}$  composites, samples were sealed in double-walled quartz capillaries with closed, rounded bottoms. The inner capillary had an outer diameter of 1.2 mm and a wall thickness of 0.1 mm, while the outer capillary had an outer diameter of 1.5 mm and a thickness of 0.1 mm. Both capillaries were approximately 50 mm in height. Samples were initially ground with a mortar and pestle to reduce particle size and to ensure homogeneous mixing of the feedstocks. A thin powder layer of approximately 1 mm was loaded into the inner capillary, followed by the insertion of quartz wool to compact the sample and restrict its movement. The inner capillary containing the sample was then inserted into the outer capillary and sealed with high-temperature epoxy resin which is stable up to  $1300^\circ\text{C}$ . The epoxy was allowed to cure fully before packaging and shipment to the beamline.

For the  $\text{UB}_4$  measurement, a different double-capillary configuration was used. These capillaries have outer diameters of 2.1 mm and 1.9 mm, respectively, with thickness of 0.2 mm with open end that allows the mounting of an alumina rod with outer diameter of  $\approx 1.8$  mm inside the capillary to

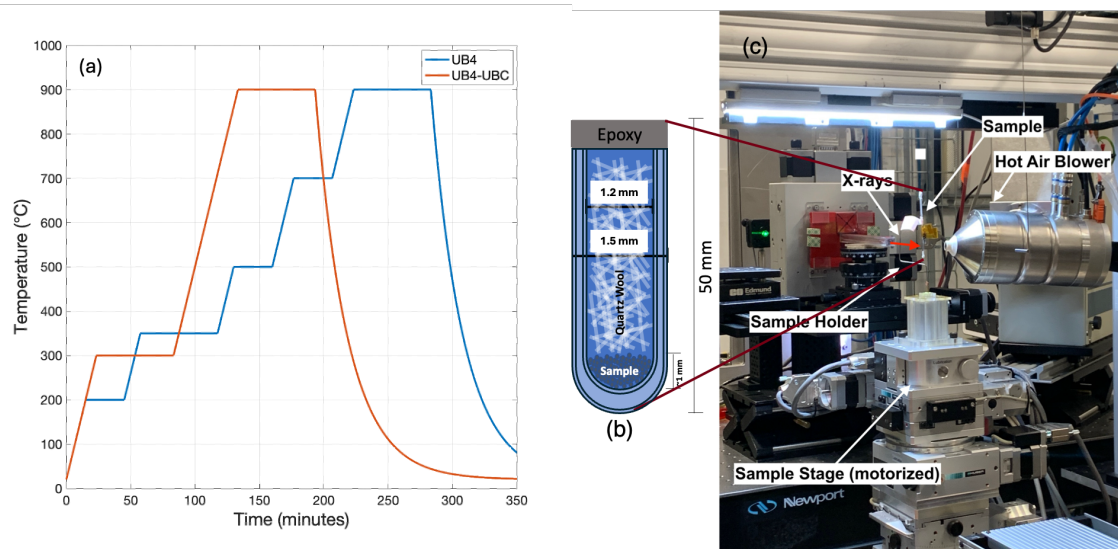


Figure 1: (a) Heating profile for synchrotron characterization of a  $UB_4$  and  $UB_4$ - $UBC$  composite sample (b) Double layer containment sketch for  $UB_4$ - $UBC$  sample in quartz capillaries (c) High temperature in situ heating XRD setup at 28-ID at NSLS II.

provide a physical buffer between the sample and the sealant. The alumina rod, inner capillary, and outer capillary were sealed together using alumina-based glue. After drying, an approximately 1 mm-thick layer of sample was loaded directly above the alumina rod and compacted with quartz wool and a tertiary quartz capillary. A final layer of alumina glue was applied to seal the assembly from the top.

The experimental setup is schematically shown in Figure 1c. Samples were heated to the desired temperatures using a hot air blower. A two-dimensional (2D) CsI flat panel area detector (Dexela 2923) with a pixel size of  $75 \mu\text{m} \times 75 \mu\text{m}$  was mounted orthogonally to the X-ray beam to collect the diffraction patterns. The wavelength of the incident X-ray beam was  $0.1811 \text{ \AA}$  ( $68.46 \text{ keV}$ ). The sample-to-detector distance was calibrated using a NIST  $LaB_6$  standard and determined to be 0.8 m. The beam spot size was  $250 \mu\text{m} \times 250 \mu\text{m}$ . The 2D diffraction patterns were cleared from electronic artifacts created by dead pixels and from the shadow of the beam stop. The detector acquisition time was set at 0.1 s. To improve the counting statistics while avoiding saturation, multiple frames were acquired and averaged. Meanwhile, the laboratory XRD (LXRD) measurements were performed using a Siemens D5000 diffractometer with  $Cu K\alpha$  radiation source ( $\lambda = 1.5418 \text{ \AA}$ ), with  $2\theta$  ranging from ranging from  $20^\circ$  to  $60^\circ$  a  $2\theta$  step size of  $0.02^\circ$ , and an acquisition time of 1 s per step.

The data analysis is automated at 28-ID-2, such that the 2D diffraction images are masked and integrated to produce the corresponding 1D diffraction patterns. The XRD patterns were indexed using JADE Pro (Materials Data, Inc.)<sup>[26]</sup> with access to the International Centre for Diffraction Data (ICDD) Powder Diffraction File (PDF)-5+ database<sup>[20]</sup>. All the XRD data analysis (Figure S1) was performed using the open-source General Structure Analysis System II (GSAS-II) software package<sup>[36]</sup>. A module in GSAS-II referred to as `GSASIIscriptable` allows for automation of refinement and is utilized in this work. The (110) and (200) peaks of alumina, resulting from the alumina rod at the base of the sample, were excluded from the fitting. The refinement results for the pristine and pre-oxidized  $UB_4$ - $UBC$  can be found in Figure S1 and S2.

### 3 Results

#### 3.1 Gibb's free energy calculations

The Gibbs free energy of reaction was calculated to show the correlation between the partial pressure of CO gas released, temperature, and spontaneity of the reactions. The Gibbs free energy for a specific reaction can be computed based on the molarity of reactants and products using Equation (2):

$$\Delta G_{\text{rxn}}(T) = \sum_p c_p \Delta G_{f,p}(T) - \sum_r c_r \Delta G_{f,r}(T) \quad (2)$$

$\Delta G_{\text{rxn}}$  is the Gibbs free energy of formation for a reactant (r) or product (p) in units of J/mol at standard pressure and C is the molar quantity of each reactant or product. When a gaseous species is present in the reactants or products, the Gibbs free energy of the reaction can be written with respect to the partial pressures of gases produced in the reaction. In the case of the synthesis

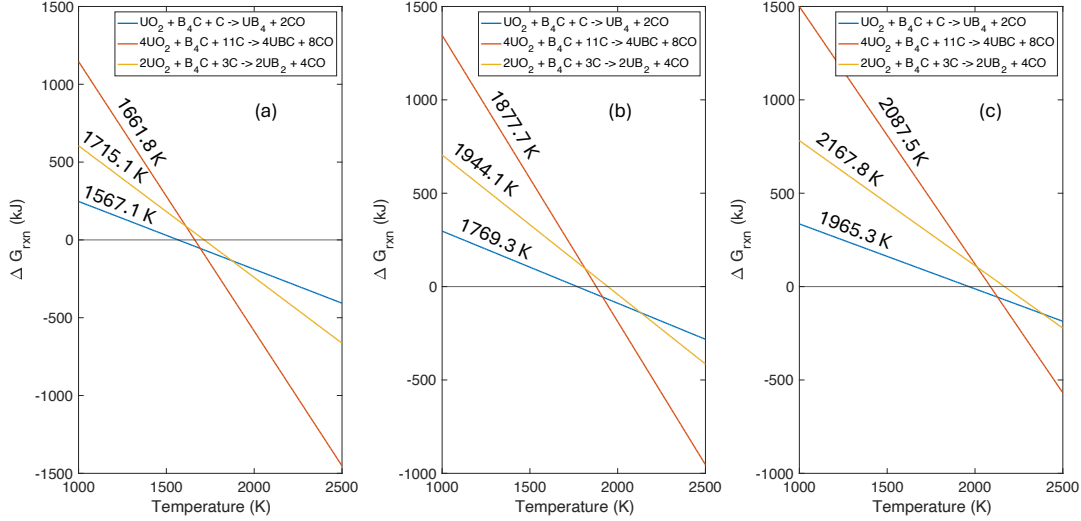
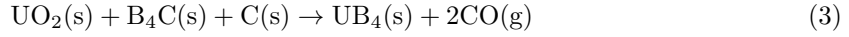


Figure 2: Temperature dependence of the Gibbs free energy of formation ( $\Delta G_{rxn}$ ) for the reactions leading to  $UB_4$ ,  $UBC$ , and  $UB_2$  formation at varying (a) low – 50 Pa, (b) intermediate – 10 kPa, and (c) high – 101 kPa  $CO$  partial pressures. At 1700 °C,  $UB_4$  and  $UBC$  formations remain spontaneous, whereas  $UB_2$  synthesis is suppressed under high  $CO$  pressure, consistent with experimental observations.

of  $UB_4$ ,  $CO$  is produced as a by-product of the carboborothermic reduction reaction:



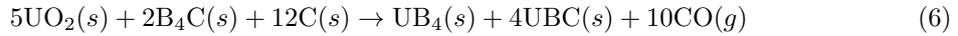
The effect of the  $CO$  partial pressure on the Gibbs free energy of reaction can be written as<sup>[38]</sup>:

$$\Delta G_{rxn, pressure} = C_{CO} RT \ln \left( \frac{P_{CO}}{101 \text{ kPa}} \right) \quad (4)$$

$R$  is the ideal gas constant given as  $8.314 \text{ JK}^{-1}\text{mol}^{-1}$ ,  $C_{CO}=2$  for the synthesis of  $UB_4$  and  $P_{CO}$  is the partial pressure of  $CO$  in kPa. Therefore, for the synthesis of  $UB_4$ , the Gibbs free energy of reaction may be given as:

$$\Delta G_{rxn}(T, P_{CO}) = C_{CO} RT \ln \left( \frac{P_{CO}}{101 \text{ kPa}} \right) + \Delta G(T) \quad (5)$$

The temperature-dependent Gibbs free energy of formation was extracted from the thermochemical data of pure substances for  $UO_2$ ,  $B_4C$ ,  $C$ ,  $CO$ , and  $UB_4$ <sup>[1]</sup>. This data was fitted to a first-degree polynomial, then extrapolated to the temperature range used during synthesis. It is hypothesized that the formation of a  $UB_4$ – $UBC$  composite from a  $UO_2$ ,  $B_4C$ , and  $C$  feedstock proceeds via the following overall reaction in a graphite crucible:



This is potentially a two-step reaction where the first is given by Equation (6) and the second is given as:



The Gibbs free energy of the reaction was calculated using Equations (6) and (7) compared with reaction for  $UB_2$  synthesis as shown in Figure 2 for three different  $CO$  partial pressures of  $CO$  gas. Meanwhile, since there is only sparse experimental data on the thermophysical properties of  $UBC$ , a simple linear fit for the Gibbs free energy of formation was performed to calculate  $\Delta G_{rxn}$  using the values  $\Delta G_f$  at 25°C and 1600°C from Rogl *et al.*<sup>[32]</sup>. The comparison in Figure 2, shows that, at  $CO$  partial pressures ranging from 50 Pa to 101 kPa, the relative spontaneity of these reactions with increasing temperature follows the order:  $T(UB_4) < T(UBC) < T(UB_2)$ . The thermodynamic stability maps (an Ellingham-type plots extended to pressure relevant gas–solid or solid–solid reactions involving gaseous species such  $CO$ ) over which the synthesis of  $UB_4$ ,  $UB_2$  and  $UBC$  is spontaneous is shown in Figure S2. These thermodynamic results corroborate experimental observations indicating that the formation of  $UB_4$  and  $UBC$  is favored under high  $CO$  partial pressures at 1700°C, whereas the synthesis of  $UB_2$  is suppressed by the excess  $CO$  atmosphere. Each line represents a possible reaction pathway involving  $UO_2$ ,  $B_4C$ , and  $C$  as starting feedstocks.

The intersection points indicate the equilibrium temperatures where  $\Delta G_{\text{rxn}}=0$ . With increasing CO partial pressure, all reactions become thermodynamically less favorable, shifting the equilibrium to higher temperatures.

## 3.2 Synthesis Results

### 3.2.1 UB<sub>4</sub> synthesis

The experimental parameter space for sintering single phase UB<sub>4</sub> was systematically explored by varying sintering environment, temperature, and time. All UB<sub>4</sub> samples were prepared using the identical pre-sinter stoichiometry of UO<sub>2</sub>:B<sub>4</sub>C:C which is equivalent to 1.00:1.04:1.00, with an excess of B<sub>4</sub>C to account for volatilization during heating. To further show the effects of the sintering crucible, a stoichiometric mixture of UO<sub>2</sub>, B<sub>4</sub>C, and C was ball-milled for 2.5 h at 330 rpm. Two samples were pressed into pellets and sintered simultaneously at 1500°C for 1 h under 100 sccm flowing argon—one in a graphite crucible and the other in an alumina crucible. XRD analysis indicated that the sample sintered in the alumina crucible comprised a single UB<sub>4</sub> phase, while the sample sintered in the graphite crucible showed a predominantly UO<sub>2</sub> and minor UBC phase respectively. The use of a graphite crucible suppressed the formation of UB<sub>4</sub> due to the excess carbon from the graphite crucible, which alters the local reaction stoichiometry. Hence, the alumina crucible was used for the remainder of the sintering experiments.

Table 1: Processing conditions and resulting dominant phases for UB<sub>4</sub> synthesis. Al\* phases originate from the alumina sample holder.

Stoichiometry (UB <sub>4</sub> : B <sub>4</sub> C: C)	Ball-milling speed (rpm, time)	Time (h)	Temperature (°C)	Dominant phases (UB <sub>4</sub> )
(1.00, 1.04, 1.00)	300, 4.5 h	1	1500	UB <sub>4</sub> , Al*
(1.00, 1.04, 1.00)	300, 4.5 h	2	1500	UB <sub>4</sub> , Al*
(1.00, 1.04, 1.00)	300, 4.5 h	3	1500	UB <sub>4</sub>
(1.00, 1.04, 1.00)	300, 4.5 h	5	1500	UB <sub>4</sub>
(1.00, 1.04, 1.00)	300, 4.5 h	1	1450	UB <sub>4</sub> , Al*
(1.00, 1.04, 1.00)	300, 4.5 h	1	1550	UB <sub>4</sub> , Al*

The time and temperature windows for UB<sub>4</sub> synthesis were further investigated after establishing synthesis conditions that produced a dominant UB<sub>4</sub> phase fraction. Six samples were prepared using the same precursor stoichiometry and were ball-milled for 4.5 h in a tungsten jar at approximately 300 rpm, ensuring comparable particle size distributions. Each mixture was pressed into a pellet under 300–400 MPa and subjected to a 5°C/min heating rate with two 30 min isotherms at 500 °C and 1000°C. The sintering conditions for each sample and the corresponding phases from XRD analysis are summarized in **Table 1**. It is important to point out that the alumina sample holder includes aluminum which is denoted as Al\* in **Table 1**.

The LXRDR results shown in Figure 3 include peaks corresponding to alumina, originating from the alumina sample holder. Initially, these were suspected to arise from a reaction between UB<sub>4</sub> and the alumina crucible. However, background scans of the XRD sample holder confirmed that the aluminum peaks originated from the holder itself due to incomplete coverage by the sparse powder. By considering the contribution of the sample holder to the LXRDR results, we found that all samples sintered at varied temperatures and durations show a dominant composition of UB<sub>4</sub>. It is suspected that some phase fraction of UO<sub>2</sub> is present within the samples but is not well resolved by the LXRDR measurement. Furthermore, overlap between the high intensity UO<sub>2</sub> (111) reflection and the UB<sub>4</sub> (210) reflection may contribute to the obscured UO<sub>2</sub> signal at this reflection. This suggests that 1 h is sufficient for the synthesis of UB<sub>4</sub> in small quantities at temperatures ranging from 1450 °C to 1500 °C.

### 3.2.2 UB<sub>4</sub>–UBC synthesis

During preliminary efforts to synthesize UB<sub>2</sub>, UB<sub>4</sub>–UBC composite samples were also formed. Subsequent analysis of these trials enabled the determination of effective stoichiometry and sintering parameters for the deliberate synthesis of UB<sub>4</sub>–UBC. The UB<sub>4</sub>–UBC composite sample was produced from a feedstock mixture of graphite, uranium dioxide and boron carbide that had been ball milled in a tungsten milling jar at a speed of 300 to 400 rpm for 2 to 2.5 h. The sample was sintered at 1700 °C under 100 sccm argon flow. The stoichiometry, sintering conditions, and resulting composition of the UB<sub>4</sub>–UBC composite are summarized in **Table 2**, along with those of the UB<sub>4</sub> sample analyzed by SXRDR for comparison.

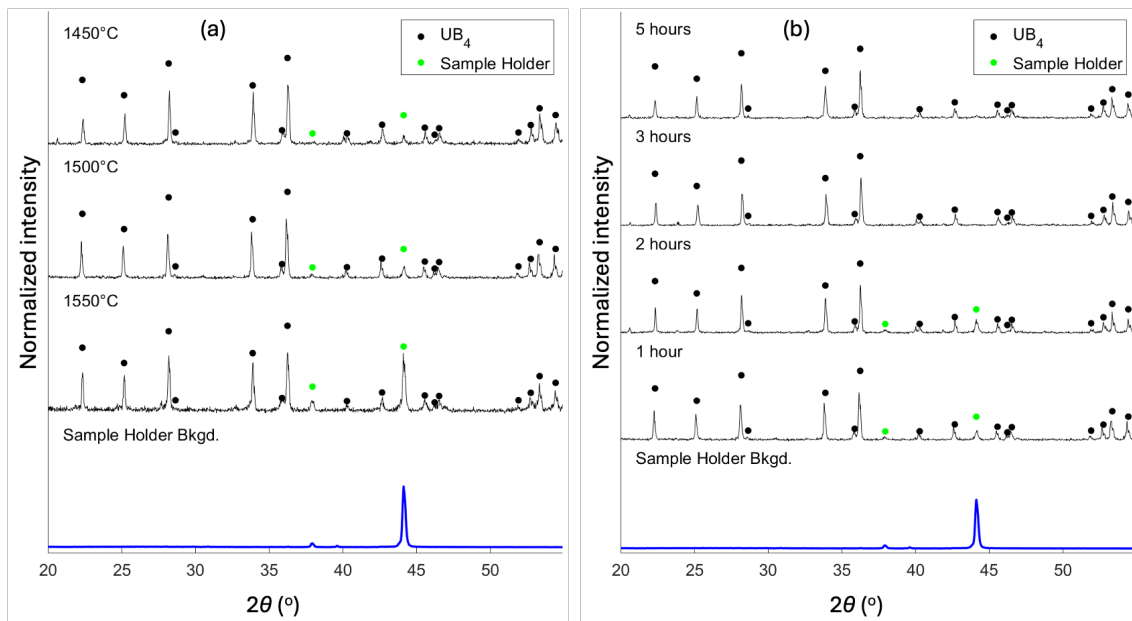
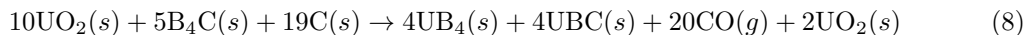


Figure 3: (a) Effect of sintering temperature on the LXR D patterns of  $UB_4$  after 1 h of sintering. (b) Effect of sintering duration on the LXR D patterns of  $UB_4$  at a fixed temperature of  $1500^\circ\text{C}$ . Peaks were indexed against PDF [01-085-4598] for  $UB_4$  taken from the International Centre of Diffraction Data (ICDD).

A  $UO_2$  phase fraction of  $\approx 10\text{ wt}\%$  was observed during the sintering of  $UB_4$ -UBC composite which may be due to partial reduction of the starting feedstock with some unreacted  $UO_2$  as shown in Equation (8):



### 3.2.3 Microstructural Characterization

The microstructural evolution of  $UB_4$  as function of sintering time is shown in Figure 4 (top) with initial particle coalescence leading to grain growth and densification. One hour of sintering shows region densification, a part of the  $UB_4$  sample also displays a highly porous morphology with partially bonded particles, which implies uneven solid-state diffusion. As the sintering duration increases from 2-3 hours, neck formation and grain coalescence become more pronounced, leading to a denser structure with improved interparticle bonding. However, after 5 h, abnormal grain growth is observed, which points to prolonged exposure at high temperatures promoting atomic scale mobility, and resulting in grain coarsening and entrapment of localized porosity within larger grains. Meanwhile, the  $UB_4$ -UBC composite sintered for 1 h as shown in Figure 4 (bottom) exhibits a noticeably finer and more homogeneous microstructure. The high-resolution SEM shows faceted grains and well-defined grain-boundary triple junctions, which is indicative of efficient diffusion and grain growth[5]. The presence of UBC appears to inhibit grain growth by acting as a diffusion barrier and stabilizing the microstructure during sintering. This effect allows for higher relative density to be achieved in a shorter sintering time compared to monolithic  $UB_4$ .

Meanwhile, elemental mapping further confirms the formation of a uniform  $UB_4$ -UBC composite. Uranium and boron are evenly distributed, while there is preferential distribution of carbon at the grain boundaries, consistent with the presence of the UBC phase. The minor oxygen signal compared to the U, C and B in the EDX map is indicative of the limited residual  $UB_2$  or surface oxidation. Overall, this shows that that excess carbon promotes formation of UBC which enhances the sintering kinetics, refines the microstructure, and minimizes the oxidation of  $UB_4$ .

Table 2: Initial stoichiometry, sintering conditions, and resulting composition of the  $UB_4$  and  $UB_4$ -UBC samples synthesized via the borocarbothermic reduction route and investigated by SXRD. Samples were sintered using a graphite crucible.

Sample	Stoichiometry (mol)			Sintering Conditions			Resulting Dominant Phases
	$UO_2$	$B_4C$	C	Temp ( $^\circ\text{C}$ )	Time (h)	Env.	
$UB_4$	1.00	1.04	1.00	1500	1	Argon	$UB_4$
$UB_4$ -UBC	2.00	1.04	3.60	1700	2	Argon	$UB_4$ , UBC, $UO_2$

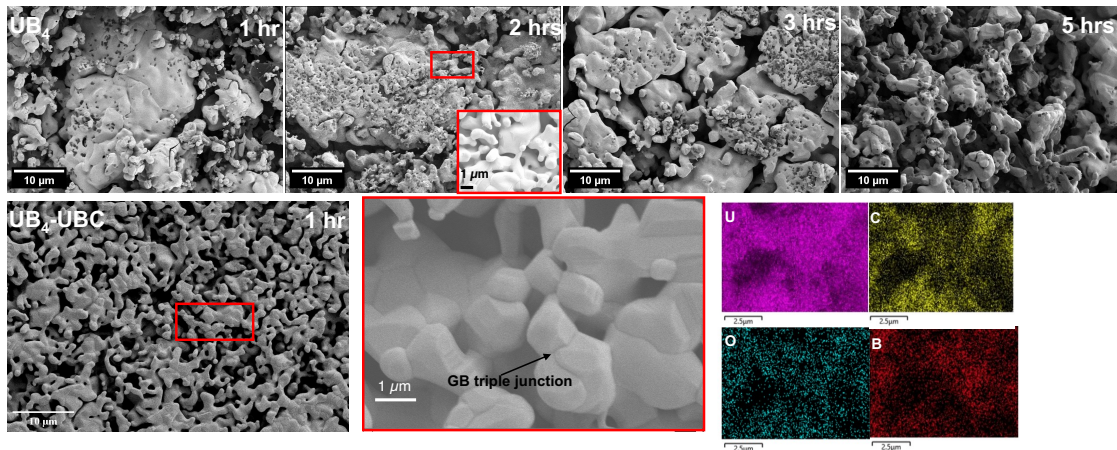


Figure 4: SEM images of sintered  $UB_4$  (top) compared with those of the  $UB_4$ - $UBC$  composite at different regions of the pellet (bottom). The red regions illustrate the coalescing grains during sintering.

## 4 Discussion

### 4.1 High temperature phase stability

The structural stability of the  $UB_4$  and  $UB_4$ - $UBC$  composite samples was investigated using the heating profiles shown in Figure 1. SXR data was collected intermittently throughout the duration of the sample heating. A comparison of the SXR data at intermittent temperatures can be observed in Figure 5. Phase fractions and lattice parameters were extracted through Rietveld refinement of the XRD data, and these values were subsequently used to calculate the volumetric thermal expansion of the  $UB_4$  and  $UBC$  phases as shown in Figure 5.

A notable phase fraction of  $Al_2O_3$  is observed in the  $UB_4$  sample which comes from the alumina rod used for the  $UB_4$  sample mounting inside the capillaries. It is important to note that a  $UB_{12}$  and a  $UO_2$  phase were observed in the  $UB_4$  sample, highlighting the capability of high intensity, high energy synchrotron X-rays to resolve minor phase fractions in high atomic density samples. These phases were not observed in the LXR measurements using the in-laboratory diffractometer due to the low signal to noise ratio. Previous work also shows the presence of minor  $UB_{12}$  phase when synthesized with a 5 mol % excess of boron carbide under the same thermal conditions[14] as used in this experiment. In Figure 5a, the diffraction peaks correspond to  $UB_4$ ,  $UB_{12}$ ,  $UO_2$ , and minor  $Al_2O_3$  phases, with  $UB_4$  peaks decreasing and  $UO_2$  peaks becoming more pronounced as temperature increases, indicating progressive oxidation. At 900 °C, the pattern shows dominant oxide phases and diminished boride peaks. Meanwhile, in Figure 5b,  $UB_4$ - $UBC$  shows a similar oxidation trend, but the presence of  $UBC$  seems to delay the onset of oxides, with  $UO_2$  peaks appearing at lower temperatures of  $\approx 195$  °C and boride peaks persisting at higher temperatures compared to pure  $UB_4$ . The results suggest that the  $UB_4$ - $UBC$  composite oxidizes more gradually over the heating profile, with phase evolution occurring at slightly lower temperatures than in the pure  $UB_4$  sample. Even though the  $UB_4$ - $UBC$  samples were sealed, it is possible that water vapor out-gassing during curing of alumina glue may contribute to oxidation behavior[15].

We have summarized the lattice parameters and phase fractions in Figure 6. At room temperature, the lattice parameters for  $UB_4$ - $UBC$  composite are similar to those of the pure  $UB_4$  phase. These results are similar to measurements by Bertaut *et al.* where  $a$  is 7.080 Å, and  $c$  is 3.978 Å[6] while Zalkin *et al.* reported  $a$  equal to 7.075 Å and  $c$  equal to 3.979 Å[41]. Additionally, the room temperature lattice parameter of the  $UBC$  phase is comparable to reported values by Rogl *et al.* where  $a$  is 3.5927 Å,  $b$  is 11.9889 Å, and  $c$  is 3.3474 Å[30]. Furthermore, the Rietveld refinement of the  $UB_4$ - $UBC$  composite indicates phase fractions of 42 wt%  $UB_4$ , 48 wt%  $UBC$ , and 10 wt%  $UO_2$ , respectively. These proportions remain stable throughout the heating process, demonstrating the thermal stability of the composite. At high temperatures, there is a slight increase in the phase fraction of  $UO_2$  while there is a corresponding decrease in the  $UB_4$  phase. For instance, in the pristine  $UB_4$  sample, at a critical temperature of about 700 °C, a rapid increase of the  $UO_2$  phase is observed. This result would suggest that the  $UB_4$  sample experienced high temperature oxidation during heating.

We calculated the coefficient of thermal expansion for the  $UB_4$  phase in the pristine  $UB_4$  sample, and for the  $UB_4$  and  $UBC$  phases in the  $UB_4$ - $UBC$  composite to understand the extent of thermal strain induced during heating. The CTE of the  $UB_4$  and  $UBC$  phases for each lattice direction are summarized in Table 3 and compared with values from previous measurements. The measured

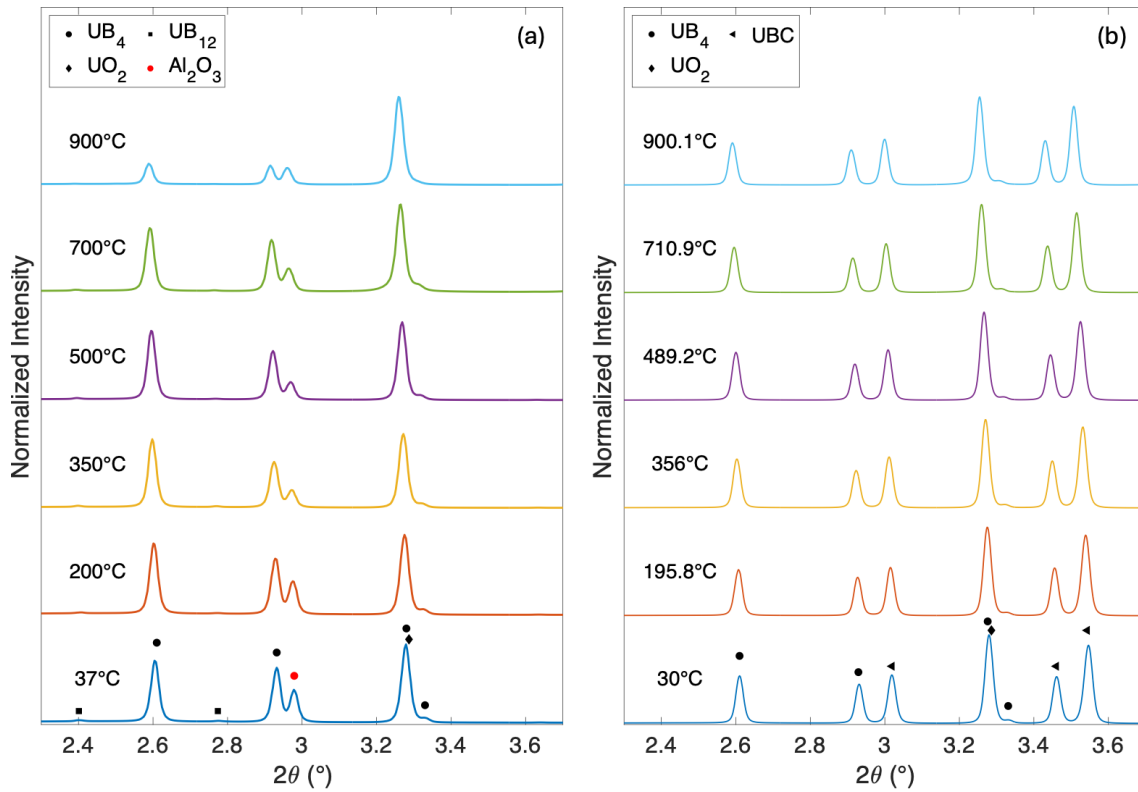


Figure 5: SXRD patterns showing the temperature-dependent phase evolution of (a)  $UB_4$  and (b)  $UB_4$ - $UBC$  during a step-by-step heating procedure in air. Diffraction patterns are displayed from room temperature to 900 °C. Peaks were indexed against PDF [01-085-4598] for  $UB_4$ , PDF [00-005-0550] for  $UO_2$ , PDF [01-083-2940] for  $UB_{12}$ ,  $Al_2O_3$  from Ishizawa et. al.<sup>35</sup>, and PDF [04-008-8907] for  $UBC$  (ICDD).

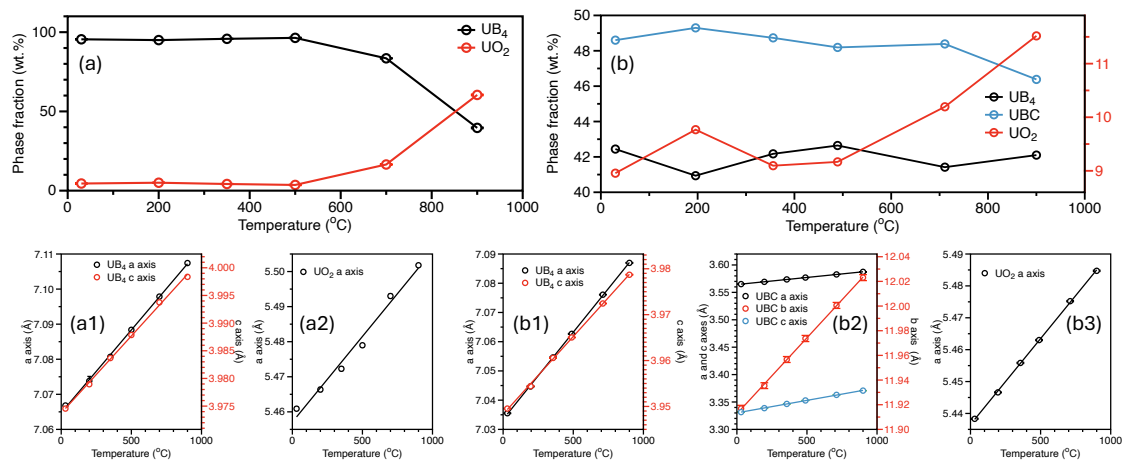


Figure 6: Temperature-dependent evolution of phase fractions and lattice parameters for pristine  $UB_4$  and  $UB_4$ - $UBC$  composite samples. (a) Phase fractions of  $UB_4$  and  $UO_2$  as a function of temperature for the pristine  $UB_4$  sample. (a1-a2) Corresponding temperature dependence of the  $UB_4$  (a and c) and  $UO_2$  (a) lattice parameters. (b) Phase fractions of  $UB_4$ ,  $UBC$ , and  $UO_2$  for the  $UB_4$ - $UBC$  composite. (b1-b3) Temperature evolution of lattice parameters for  $UB_4$  (a and c),  $UBC$  (a and c), and  $UO_2$  (a), respectively.

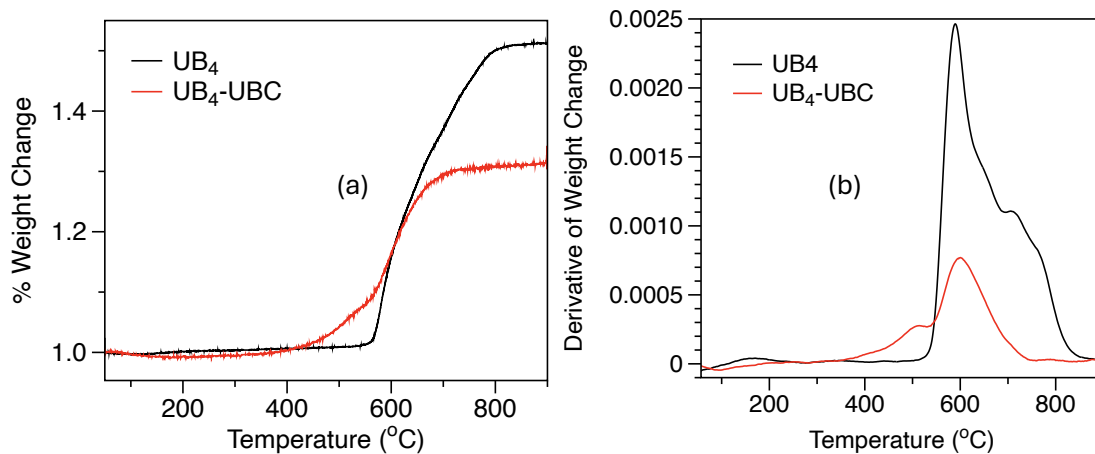


Figure 7: (a) Fractional mass change of  $UB_4$  and  $UB_4$ -UBC with temperature under flowing dry air, measured by thermogravimetric analysis (TGA). (b) The differential thermogravimetric (DTG) for  $UB_4$  and  $UB_4$ -UBC under flowing dry air, measured by thermogravimetric analysis.

directionally averaged linear coefficient of expansion was  $\approx 30\%$  greater for the  $UB_4$  phase of the  $UB_4$ -UBC composite compared with the  $UB_4$  phase of the pristine  $UB_4$  sample. Matterson *et al.* reported a value of  $7.1 \times 10^{-6} \text{ K}^{-1}$  for the  $UB_4$  phase measured by dilatometry[27] which is lower than the value calculated here from SXRD data. For the  $UB_4$ -UBC composite, a directionally averaged CTE of  $10.75 \times 10^{-6} \text{ K}^{-1}$  was calculated for the UBC phase.

Table 3: Mean linear coefficients of thermal expansion for the  $UB_4$  phase of the pristine  $UB_4$  and the  $UB_4$  and UBC phases of the  $UB_4$ -UBC composite compared to previous studies.

Sample	Phase	a-axis ( $\times 10^{-6} \text{ K}^{-1}$ )	b-axis ( $\times 10^{-6} \text{ K}^{-1}$ )	c-axis ( $\times 10^{-6} \text{ K}^{-1}$ )	Averaged ( $\times 10^{-6} \text{ K}^{-1}$ )	Measurement technique
Pristine $UB_4$	$UB_4$	6.22(28)	–	7.57(47)	6.67	Diffraction
$UB_4$ -UBC	UBC	7.44(16)	10.45(40)	14.35(52)	10.75	Diffraction
$UB_4$ -UBC	$UB_4$	8.43(24)	–	8.65(46)	8.50	Diffraction
Pristine $UB_4$	$UB_4$	–	–	–	7.1	Dilatometry[27]
Pristine $UB_4$	$UB_4$	–	–	–	10.0	Dilatometry[22]
Pristine $UB_2$	$UB_2$	9.00	–	8.00	7.7	Diffraction[3]
Pristine $UB_2$	$UB_2$	–	–	–	9.0	Dilatometry[22]

## 4.2 *In situ* high temperature oxidation behavior

### 4.2.1 Thermogravimetric analysis

The  $UB_4$  and the  $UB_4$ -UBC composite were investigated via thermogravimetric analysis. The measurement and data analysis methodology for rendering fractional mass changes with evolving temperature are described in Section 2.2. The results for the fractional mass change under flowing dry air for the  $UB_4$  sample and the  $UB_4$ -UBC composite sample are displayed in Figure 7a. The first derivative of the mass change for each sample is displayed in Figure 7b.

Figure 7 displays the thermogravimetric (TGA) curves for pristine  $UB_4$  and the  $UB_4$ -UBC composite under an oxidizing atmosphere. Pristine  $UB_4$  demonstrates negligible mass change up to  $\approx 550^\circ\text{C}$  to  $580^\circ\text{C}$ , after which a sharp increase in weight occurs, resulting in a total mass gain of  $\approx 50\%$  to  $52\%$  at  $900^\circ\text{C}$ . This pronounced weight gain signifies rapid oxidation at elevated temperatures and suggests the formation of  $U_3O_8$  and  $B_2O_3$  phases as shown in XRD phase analysis. This is consistent with Guo *et al.* who observed the formation of  $U_3O_8$  in the temperature range of  $400^\circ\text{C}$  to  $600^\circ\text{C}$  and  $UB_2O_6$  at  $600^\circ\text{C}$  to  $800^\circ\text{C}$  [14]. In contrast, the  $UB_4$ -UBC composite shows an earlier onset of weight gain around  $450^\circ\text{C}$  to  $500^\circ\text{C}$ , but the mass increase proceeds more gradually compared to  $UB_4$ . The total weight gain of the composite is within the range of  $\approx 30\%$  to  $32\%$  at  $900^\circ\text{C}$ , indicating a substantial reduction relative to pristine  $UB_4$ . These results indicate that the UBC phase effectively suppresses high-temperature oxidation and limits oxygen uptake.

The corresponding differential thermogravimetric (DTG) curves are presented in Figure 7b. Pristine  $UB_4$  displays a sharp and intense oxidation peak centered at  $590^\circ\text{C}$  to  $620^\circ\text{C}$ , with a maximum derivative weight change of about  $2.4 \times 10^{-3}$ , indicating a rapid oxidation rate. Additional shoulders at higher temperatures suggest multi-step oxidation processes.

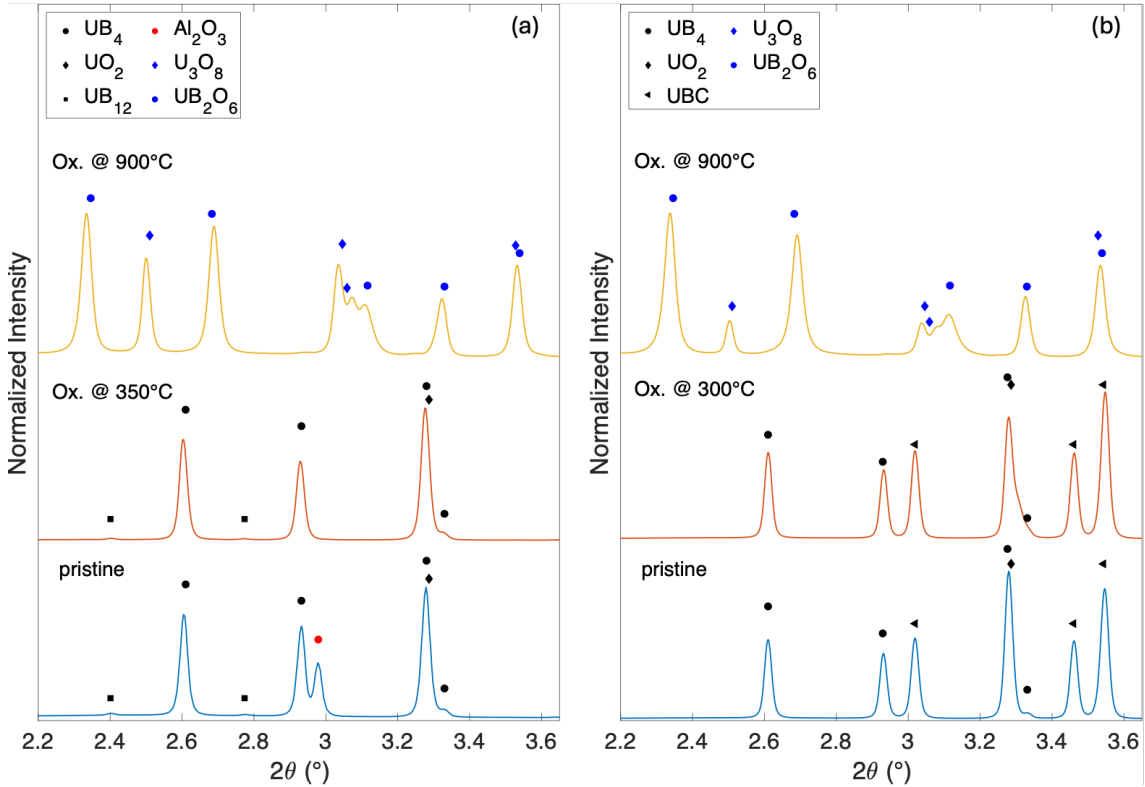
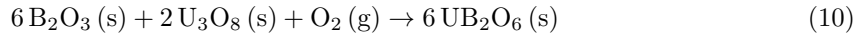
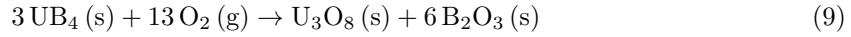


Figure 8: This figure shows XRD patterns comparing the oxidation behavior of (a) UB<sub>4</sub> and (b) UB<sub>4</sub>-UBC composites under different atmospheric conditions (dry versus moist air) and temperatures. Peaks were indexed against PDF [01-085-4598] for UB<sub>4</sub>, PDF [00-005-0550] for UO<sub>2</sub>, PDF [01-083-2940] for UB<sub>12</sub>, Al<sub>2</sub>O<sub>3</sub> from Ishizawa et. al.[17], PDF [01-078-6745] for U<sub>3</sub>O<sub>8</sub>, and PDF [04-012-6543] for UB<sub>2</sub>O<sub>6</sub> taken from the ICDD.

This corresponds to the formation of U<sub>3</sub>O<sub>8</sub> and B<sub>2</sub>O<sub>3</sub> in the first step followed by a second step where excess U<sub>3</sub>O<sub>8</sub> react with B<sub>2</sub>O<sub>3</sub> to form UB<sub>2</sub>O<sub>6</sub> as follows:

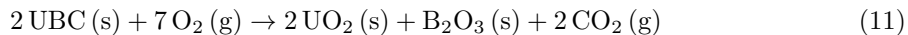


Meanwhile, the UB<sub>4</sub>-UBC composite exhibits a broader and significantly lower-intensity peak, with a maximum of  $\approx 0.75 \times 10^{-3}$ , confirming a markedly reduced oxidation rate and more controlled reaction kinetics. The results suggest that the incorporation of UBC into UB<sub>4</sub> leads to both a reduction in the oxidation rate and a decrease in total mass gain. This enhanced oxidation resistance is attributed to the formation of carbon- and boron-rich phases that impede oxygen diffusion and facilitate the development of a protective surface layer, thereby stabilizing the composite at elevated temperatures.

#### 4.2.2 *In situ* phase stability of pre-oxidized UB<sub>4</sub>-UBC

A microgram quantity of the synthesized UB<sub>4</sub> and UB<sub>4</sub>-UBC was oxidized to 300 °C / 350 °C and 900 °C, following the methodology described in Section 2.2. *In situ* high-temperature SXRD measurements were performed to identify and index the phases present and to determine their corresponding crystal structures. The resulting indexed peaks of the oxidized UB<sub>4</sub> and UB<sub>4</sub>-UBC composite samples are compared in Figure 8. It should be noted again that the UB<sub>4</sub> sample was oxidized in dry air and the UB<sub>4</sub>-UBC composite in moist air.

Oxidation studies revealed that both UB<sub>4</sub> and UB<sub>4</sub>-UBC composite samples transformed predominantly into U<sub>3</sub>O<sub>8</sub> and UB<sub>2</sub>O<sub>6</sub> at 900 °C, consistent with previously reported phases during high-temperature oxidation of UB<sub>4</sub><sup>16</sup>. The results further indicate that oxidation of the UBC phase proceeds through carbon volatilization, leading to the release of gaseous CO and CO<sub>2</sub>. The onset of rapid oxidation was observed between 300 °C to 350 °C, extending up to approximately 900 °C, in agreement with the TGA data. Our results suggest that UB<sub>4</sub> exhibits stability in oxidizing environments up to roughly 350 °C, whereas the UB<sub>4</sub>-UBC composite remains stable only up to  $\approx 300$  °C.



The lattice parameters of the pre-oxidized  $\text{UB}_4$  phase in dry air at  $350^\circ\text{C}$  are  $a$  equal to  $7.070(72) \text{ \AA}$  and  $c$  equal to  $3.975(10) \text{ \AA}$ . These lattice parameters exceed those of the pristine sample by less than  $\approx 1\%$ . Similarly, the relative phase wt% increased from  $4.5\%$  to  $5.5\%$  following the oxidation experiments. Meanwhile, the  $\text{UBC-UB}_4$  composite observed a much greater increase in lattice volume following oxidation to  $300^\circ\text{C}$  in moist air. The lattice parameters of the  $\text{UB}_4$  phase were determined to be  $a = 7.075(3) \text{ \AA}$  and  $c = 3.973(3) \text{ \AA}$ , while those of the  $\text{UBC}$  phase were found to be  $a = 3.586(3) \text{ \AA}$ ,  $b = 11.986(3) \text{ \AA}$ , and  $c = 3.350(3) \text{ \AA}$ . There is a marginal increase in the relative phase fraction of  $\text{UO}_2$  from  $9\%$  to  $10\%$ . The samples oxidized to  $900^\circ\text{C}$  were refined for the resulting phase fractions and the  $\text{UB}_2\text{O}_6$  lattice parameters. For the pristine  $\text{UB}_4$  sample oxidized to  $900^\circ\text{C}$  in dry air, the  $\text{UB}_2\text{O}_6$  lattice parameters were determined such that  $a$  is  $12.502(3) \text{ \AA}$ ,  $b$  is  $4.184(4) \text{ \AA}$ , and  $c$  is  $10.490(2) \text{ \AA}$ . Similarly, for the  $\text{UB}_4\text{-UBC}$  composite oxidized to  $900^\circ\text{C}$  in moist air, the lattice parameters were determined such that  $a$  is  $12.430(4) \text{ \AA}$ ,  $b$  is  $4.162(4) \text{ \AA}$ , and  $c$  is  $10.440(4) \text{ \AA}$  which is notably smaller than the parameters measured for the oxidized  $\text{UB}_4$  sample.

To further understand the high-temperature thermal stability of the  $\text{UB}_4\text{-UBC}$  phase, we heated the sample at a rate of  $10^\circ\text{C min}^{-1}$  while cooling was uncontrolled. We observed a minor  $\text{UO}_2$  phase that persisted throughout the heating and cooling process, as shown in Figure 9. The overlapping  $\text{UB}_4$  and  $\text{UO}_2$  phases show a diffraction peak shift toward lower  $2\theta$  (Figure 9a1), corresponding to lattice expansion as the temperature increases. This suggests that there is a thermal dilation of the  $\text{UB}_4$ ,  $\text{UBC}$ , and  $\text{UO}_2$  phases. The extent of the shift indicates that the phases have different thermal expansion coefficients, as shown in Table 4. Furthermore, during the cooling stage, the diffraction peak shifted towards higher  $2\theta$  values, which means that there is lattice contraction, as shown in Figure 9a2. The asymmetric shifting of the peaks may be due to residual strain, microstructural distortion, or irreversible phase evolution resulting from oxidation or partial phase decomposition[33, 42].

The resulting relative weight percentages of the dominant phases  $\text{UB}_2\text{O}_6$  and  $\text{U}_3\text{O}_8$  in the samples oxidized to  $900^\circ\text{C}$  are presented in Figure S3. By nature of the different initial phase composition and the differing oxidation conditions, the phase fraction of  $\text{U}_3\text{O}_8$  is  $\approx 15\%$  greater in the  $\text{UB}_4$  sample as compared to the  $\text{UB}_4\text{-UBC}$  sample. Considering the reaction products and the oxidation peaks in the TGA measurements, the reaction of  $\text{UB}_4\text{-UBC}$  is likely to have proceeded at a lower temperature than that of the  $\text{UB}_4$  composite. The pre-oxidized sample predominantly contains  $\text{UB}_2\text{O}_6$  and  $\text{U}_3\text{O}_8$ , which increase gradually, as shown by the peaks in Figure 9b. This implies progressive oxidation of the uranium boride phases. A further closer look at the diffraction patterns shown in Figure 9b1 – b2, is consistent with similar behavior during the oxidation of  $\text{UB}_2$  in flowing synthetic air[29]. In our case, our sample was sealed with epoxy which expels oxygen at high temperature, serving as the precursor for oxidation. The systematic increase in intensity of the oxide peaks reflects crystallization and growth of these phases during oxidation.

While the ATFs concepts have promising high thermal conductivity and high uranium loading, high temperature oxidation in steam and air is still a concern. The oxidation of uranium nitride[18], uranium carbide[11], uranium diboride, and its composite[39, 29, 37] have been investigated using TGA and differential scanning calorimetry analysis. The oxidation behavior of uranium borides, carbides, silicides, and nitrides have been investigated under air and steam atmospheres, as summarized in Table 4. The onset of oxidation depends strongly on composition and oxidation environments. The  $\text{UC}$  starts to oxidize from  $264^\circ\text{C}$  in air[12] while the oxidation of  $\text{UB}_2$  is close to  $\approx 700^\circ\text{C}$  in synthetic air[29]. Meanwhile,  $\text{UB}_4\text{-UBC}$  composite exhibited the lower oxidation onset compared to  $\text{UB}_2$  and  $\text{UB}_4$ , which is due to the multiphase interfaces that may lead to rapid pulverization of the  $\text{B}_2\text{O}_3$  formed in the early stage of oxidation.

## 5 Conclusions

In this work, we synthesized  $\text{UB}_4$  and  $\text{UB}_4\text{-UBC}$  composite via an industrially scalable carboborothermic reduction of a  $\text{UO}_2\text{-B}_4\text{C-C}$  feedstock at temperatures between  $1450^\circ\text{C}$  to  $1700^\circ\text{C}$ . A systematic optimization of sintering conditions is evaluated for  $\text{UB}_4$  and  $\text{UB}_4\text{-UBC}$  synthesis. The phase compositions were verified by laboratory XRD. The results indicate that high-purity  $\text{UB}_4$  can be produced at  $1450^\circ\text{C}$  to  $1550^\circ\text{C}$  with sintering durations of 1 h to 5 h, when employing a stoichiometric excess  $\text{B}_4\text{C}$  feedstock. Similarly, synthesis at  $1700^\circ\text{C}$  with excess graphite and  $\text{UO}_2$  resulted in the formation of a  $\text{UB}_4\text{-UBC}$  composite. The  $\text{UB}_4\text{-UBC}$  has a higher uranium loading than monolithic  $\text{UB}_4$ , comparable to  $\text{UO}_2$ . The  $\text{UB}_4$  sample synthesized at  $1500^\circ\text{C}$  for 1 h, together

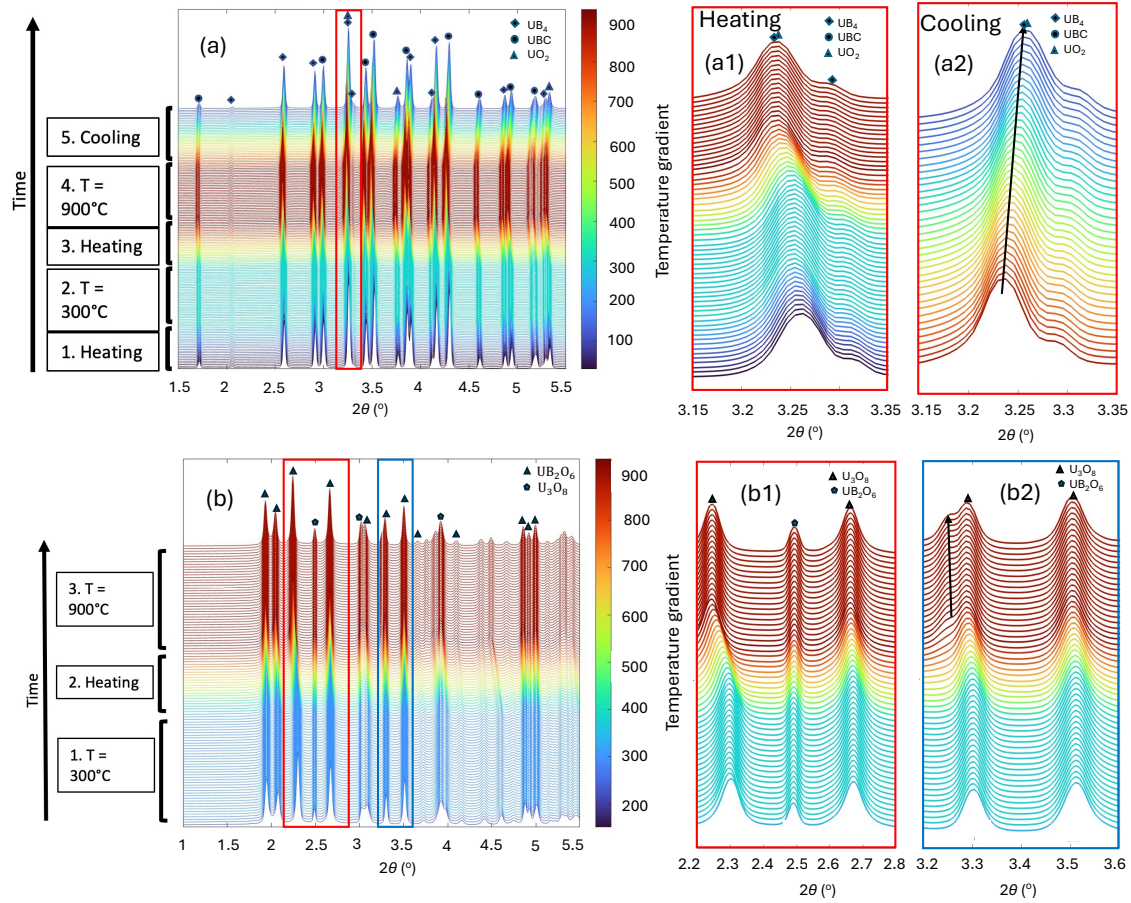


Figure 9: In situ SXR patterns showing the thermal stability of pristine and pre-oxidized of  $UB_4$ - $UBC$ . (a) Contour plots illustrate diffraction intensity as a function of temperature and  $2\theta$ , highlighting the sequential phase transitions during heating and cooling. Enlarged regions show the formation and evolution of  $UO_2$ ,  $UBC$ , and  $UB_4$  during (a1) heating (a2) cooling. (b) XRD as a function of temperature highlighting the sequential phase transitions during heating. The heating shows the persistence of oxide phases ( $UB_2O_6$ ,  $U_3O_8$ ) after high-temperature oxidation. (b1) and (b2) The intensity of the XRD peak as a function of temperature shows the progressive oxidation and boron loss leading to  $U_3O_8$  and  $UB_2O_6$  formation at elevated temperatures.

Table 4: Onset of oxidation temperature, oxidation environments, phase composition, and uranium loading of  $UB_4$ ,  $UB_4$ - $UBC$ ,  $UB_2$ ,  $UN$ ,  $UC$  and other uranium borides-containing composites.

Sample	Onset of oxidation Temperature ( $^{\circ}C$ )	Oxidation Environment	Oxidation products	Uranium loading ( $g\ cm^{-3}$ )
$UB_4$	550	Synthetic air	$UB_2O_6$ , $U_3O_8$ , $UO_2$	7.94
$UB_4$ - $UBC$	400	Ambient air	$UB_2O_6$ , $U_3O_8$	$\sim 9.5$
$UB_2$ [29]	534-692	Synthetic air	$UB_2O_6$ , $U_3O_8$ , $UO_2$	11.7
$UC$ [11]	264	Synthetic air	$U_2C_3$ , $UO_2$ , $U_3O_8$	12.98
50 wt% $UB_2$ -50 wt% $U_3Si_2$ [39]	548, 575	Steam	$UO_2$ , $U_3Si_2H_2$	-
10 wt% $UB_2$ -90 wt% $U_3Si_2$ [39]	553	Steam	$UO_2$ , $U_3Si_2H_2$	-
$UN$ -5, 25, 50 wt% $UB_2$ [37]	500-600	Steam	$U_2N_3$ , $UO_2$ , $B_2O_3$	-
$UN$ [18]	400-500	Steam	$UO_2$ , $U_3O_8$	13.51

with the  $\text{UB}_4\text{-UBC}$  composite ( $\text{UB}_4: \text{UBC} \approx 4 : 5$ ) containing a minor  $\text{UO}_2$  impurity phase, were further characterized by *in situ* high temperature SXRD analysis from room temperature to  $900^\circ\text{C}$ . The room temperature lattice parameters and linear thermal expansion coefficients were determined for the relevant phases. Notable differences in the  $\text{UB}_4$  phase expansion coefficient were observed between the two samples, which is due to anisotropy in the  $c/a$  ratio.

The oxidation behavior of the composites was investigated using TGA and subsequent post-oxidation structural characterization. The TGA results indicated oxidation onset temperatures of approximately  $400^\circ\text{C}$  for the  $\text{UB}_4\text{-UBC}$  composite and  $550^\circ\text{C}$  for the  $\text{UB}_4$  sample. While there is a relatively early onset of oxidation in  $\text{UB}_4\text{-UBC}$  compared to  $\text{UB}_4$ , the progression of oxidation is slowed down by the UBC phase as observed in the phase fractions of the  $\text{U}_3\text{O}_8$  and  $\text{UB}_2\text{O}_6$  in the *in situ* SXRD analysis.  $\text{UB}_4\text{-UBC}$  and  $\text{UB}_4$  display desirable attributes for an accident tolerant nuclear fuel, with promising oxidation behavior highlighted in this study. While this study provided insight into the synthesis, structural stability, and oxidation behavior of a novel  $\text{UB}_4\text{-UBC}$  composite and closed the knowledge gap regarding  $\text{UB}_4$ , future studies should focus on further *in situ* study of  $\text{UB}_4$  and  $\text{UB}_4\text{-UBC}$  oxidation behavior under accident scenarios to gain an understanding of the oxidation reaction kinetics.

## 6 Acknowledgement

This work was funded by the Faculty Startup Fund and Research Support Committee grant from the Massachusetts Institute of Technology. E.J. acknowledges support from the John Hardwick Career Development Chair and R.M. acknowledges the Theos J. Thompson memorial fellowship. This research used beamline 28-ID-2 (XPD) of the National Synchrotron Light Source II, a US DOE Office of Science user facility operated for the DOE Office of Science by Brookhaven National Laboratory under contract number DE-SC0012704; This research utilized resources at XPD beamline of NSLS-II that were partially supported by the U.S. Department of Energy, Office of Nuclear Energy under DOE Idaho Operations Office Contract DE-AC07-051D14517 as part of Nuclear Science User Facilities experiment (#24-4876).

## References

- [1] I. Barin and G. Platzki. *Thermochemical Data of Pure Substances*. Vol. 304. Weinheim: VCH, 1989.
- [2] J. Bauer, J.-F. Halet and J.-Y. Saillard. ‘Rare earth metal borocarbides: Examples of coordination compounds in solid-state chemistry1Dedicated to Professor Roald Hoffmann on the occasion of his 60th birthday.1’. In: *Coordination Chemistry Reviews* 178-180 (1998), pp. 723–753. DOI: [https://doi.org/10.1016/S0010-8545\(98\)00106-4](https://doi.org/10.1016/S0010-8545(98)00106-4).
- [3] G. Beckman and R. Kiessling. ‘Thermal Expansion Coefficients for Uranium Boride and  $\beta$ -Uranium Silicide’. In: *Nature* 178.4546 (1956), pp. 1341–1341. DOI: [10.1038/1781341a0](https://doi.org/10.1038/1781341a0).
- [4] P. K. Bhowmik, P. Sabharwall, B. J. Heidrich and R. Howard. *Accelerating Nuclear Fuels and Materials Qualification by Multi-Level Irradiation Experiment Campaign*. Tech. rep. Idaho Falls, ID, United States: Idaho National Laboratory (INL), 2023.
- [5] B. Bian, S. Taheriniya, G. M. Muralikrishna, S. Sen, C. Gammer, I. Steinbach, S. V. Divinski and G. Wilde. ‘Coupling of alloy chemistry, diffusion and structure by grain boundary engineering in Ni–Cr–Fe’. In: *Acta Materialia* 264 (2024), p. 119602. DOI: <https://doi.org/10.1016/j.actamat.2023.119602>.
- [6] P. Blum and F. Bertaut. ‘Contribution à l’étude des borures à teneur élevée en bore’. In: *Acta Crystallographica* 7.1 (Jan. 1954), pp. 81–86. DOI: [10.1107/S0365110X54000151](https://doi.org/10.1107/S0365110X54000151).
- [7] P. Burr, E. Kardoulaki, R. Holmes and S. Middleburgh. ‘Defect evolution in burnable absorber candidate material: Uranium diboride, UB2’. In: *Journal of Nuclear Materials* 513 (2019), pp. 45–55. DOI: <https://doi.org/10.1016/j.jnucmat.2018.10.039>.
- [8] J. Carmack, Frank, S. M. Bragg-Sitton and L. Lance. *Overview of the U.S. DOE Accident Tolerant Fuel Development Program*. 2013.
- [9] C. Degueldre, J. Bertsch and M. Martin. ‘Post irradiation examination of nuclear fuel: Toward a complete analysis’. In: *Progress in Nuclear Energy* 92 (2016), pp. 242–253. DOI: <https://doi.org/10.1016/j.pnucene.2016.03.025>.
- [10] R. Faibish. *Accelerated Fuel Qualification White Paper*. Tech. rep. Accelerated Fuel Qualification Working Group White Paper Task Force, 2021.
- [11] C. Gasparrini, R. Podor, O. Fiquet, M. Rushton and W. Lee. ‘On the oxidation and ignition of uranium carbide fragments in air and comparison with zirconium carbide oxidation’. In: *Journal of Nuclear Materials* 592 (2024), p. 154944. DOI: <https://doi.org/10.1016/j.jnucmat.2024.154944>.
- [12] V. G. Goncharov, J. Liu, A. Strzelecki, A. van Veelen, C. Benmore, H. Boukhalfa, J. T. White, H. Xu and X. Guo. ‘Energetics of oxidation and formation of uranium monocarbide’. In: *Journal of Nuclear Materials* 581 (2023), p. 154446. DOI: <https://doi.org/10.1016/j.jnucmat.2023.154446>.
- [13] A. Gonzales, J. K. Watkins, A. R. Wagner, B. J. Jaques and E. S. Sooby. ‘Challenges and opportunities to alloyed and composite fuel architectures to mitigate high uranium density fuel oxidation: uranium silicide’. In: *Journal of Nuclear Materials* 553 (2021), p. 153026. DOI: <https://doi.org/10.1016/j.jnucmat.2021.153026>.
- [14] H. Guo, J. Wang, D. Chen, W. Tian, S. Cao, D. Chen, C. Tan, Q. Deng and Z. Qin. ‘Boro/carbothermal reduction synthesis of uranium tetraboride and its oxidation behavior in dry air’. In: *Journal of the American Ceramic Society* 102.3 (2019), pp. 1049–1056. DOI: <https://doi.org/10.1111/jace.15987>. eprint: <https://ceramics.onlinelibrary.wiley.com/doi/pdf/10.1111/jace.15987>.
- [15] *High Temperature Ceramic Adhesives*. Technical Bulletin A2-S1. Manufacturer technical bulletin.
- [16] International Atomic Energy Agency. *Thermophysical Properties of Materials for Nuclear Engineering: A Tutorial and Collection of Data*. Nuclear Power Technology Development Section. Vienna, Austria, 2008.
- [17] N. Ishizawa, T. Miyata, I. Minato, F. Marumo and S. Iwai. ‘A structural investigation of  $\alpha$ -Al<sub>2</sub>O<sub>3</sub> at 2170 K’. In: *Acta Crystallographica Section B* 36.2 (Feb. 1980), pp. 228–230. DOI: [10.1107/S0567740880002981](https://doi.org/10.1107/S0567740880002981).

- [18] M. Jolkkonen, P. Malkki, K. Johnson and J. Wallenius. ‘Uranium nitride fuels in superheated steam’. In: *Journal of Nuclear Science and Technology* 54.5 (2017), pp. 513–519. DOI: [10.1080/00223131.2017.1291372](https://doi.org/10.1080/00223131.2017.1291372). eprint: <https://doi.org/10.1080/00223131.2017.1291372>.
- [19] E. Jossou, L. Malakkal, B. Szpunar, D. Oladimeji and J. A. Szpunar. ‘A first principles study of the electronic structure, elastic and thermal properties of UB2’. In: *Journal of Nuclear Materials* 490 (2017), pp. 41–48. DOI: <https://doi.org/10.1016/j.jnucmat.2017.04.006>.
- [20] S. N. Kabekkodu, A. Dosen and T. N. Blanton. ‘PDF-5+: A Comprehensive Powder Diffraction File for Materials Characterization’. In: *Powder Diffraction* 39.2 (2024), pp. 47–59. DOI: [10.1017/S0885715624000150](https://doi.org/10.1017/S0885715624000150).
- [21] E. Kardoulaki, D. Frazer, J. White, U. Carvajal, A. Nelson, D. Byler, T. Saleh, B. Gong, T. Yao, J. Lian and K. McClellan. ‘Fabrication and thermophysical properties of UO<sub>2</sub>-UB<sub>2</sub> and UO<sub>2</sub>-UB<sub>4</sub> composites sintered via spark plasma sintering’. In: *Journal of Nuclear Materials* 544 (2021), p. 152690. DOI: <https://doi.org/10.1016/j.jnucmat.2020.152690>.
- [22] E. Kardoulaki, J. White, D. Byler, D. Frazer, A. Shivprasad, T. Saleh, B. Gong, T. Yao, J. Lian and K. McClellan. ‘Thermophysical and mechanical property assessment of UB<sub>2</sub> and UB<sub>4</sub> sintered via spark plasma sintering’. In: *Journal of Alloys and Compounds* 818 (2020), p. 153216. DOI: <https://doi.org/10.1016/j.jallcom.2019.153216>.
- [23] N. R. Koenig and B. A. Webb. *Properties of Ceramic and Cermet Fuels for Sodium Graphite Reactors*. Tech. rep. Atomics International, 1960.
- [24] M. Lang, C. L. Tracy, R. I. Palomares, F. Zhang, D. Severin, M. Bender, C. Trautmann, C. Park, V. B. Prakapenka, V. A. Skuratov and R. C. Ewing. ‘Characterization of ion-induced radiation effects in nuclear materials using synchrotron x-ray techniques’. In: *Journal of Materials Research* 30.9 (May 2015), pp. 1366–1379. DOI: [10.1557/jmr.2015.6](https://doi.org/10.1557/jmr.2015.6).
- [25] W. Lyon and W. Baily. ‘The solid-liquid phase diagram for the UO<sub>2</sub>-PuO<sub>2</sub> system’. In: *Journal of Nuclear Materials* 22.3 (1967), pp. 332–339. DOI: [https://doi.org/10.1016/0022-3115\(67\)90051-7](https://doi.org/10.1016/0022-3115(67)90051-7).
- [26] Materials Data, Inc. *JADE Pro*. X-ray diffraction analysis software. Materials Data, Inc., 2023.
- [27] K. J. Matterson and H. Jones. ‘A STUDY OF THE TETRABORIDES OF URANIUM AND THORIUM’. In: *Trans. Brit. Ceram. Soc.* Vol: 60 (July 1961).
- [28] A. Menovsky, J. Franse and J. Klaasse. ‘The crystal growth of uranium tetraboride UB<sub>4</sub> from the melt’. In: *Journal of Crystal Growth* 70.1 (1984), pp. 519–522. DOI: [https://doi.org/10.1016/0022-0248\(84\)90311-7](https://doi.org/10.1016/0022-0248(84)90311-7).
- [29] Q. Mistarihi, F. Martini, J. Buckley, S. Middleburgh, T. Abram and J. Turner. ‘The oxidation of uranium diboride in flowing air atmospheres’. In: *Journal of Nuclear Materials* 580 (2023), p. 154417. DOI: <https://doi.org/10.1016/j.jnucmat.2023.154417>.
- [30] P. Rogl. ‘Actinoidmetal Boron Carbides’. In: *The Physics and Chemistry of Carbides, Nitrides and Borides*. Springer, 1990, pp. 269–277.
- [31] P. Rogl, B. Rupp, I. Felner and P. Fischer. ‘Crystal Chemistry and Magnetism of Ternary Actinoid Boron Carbides UB<sub>1-x</sub>C<sub>1+x</sub> and U<sub>1-x</sub>M<sub>x</sub>B<sub>2</sub>C with M = Sc, Lu, and Th’. In: *Journal of Solid State Chemistry* 104.2 (1993), pp. 377–390. DOI: <https://doi.org/10.1006/jssc.1993.1173>.
- [32] P. Rogl, J. Bauer and J. Debuigne. ‘The ternary system uranium-boron-carbon’. In: *Journal of Nuclear Materials* 165.1 (1989), pp. 74–82. DOI: [https://doi.org/10.1016/0022-3115\(89\)90504-7](https://doi.org/10.1016/0022-3115(89)90504-7).
- [33] G. Rousseau, L. Desgranges, F. Charlot, N. Millot, J. Nièpce, M. Pijolat, F. Valdivieso, G. Baldinozzi and J. Bézar. ‘A detailed study of UO<sub>2</sub> to U<sub>3</sub>O<sub>8</sub> oxidation phases and the associated rate-limiting steps’. In: *Journal of Nuclear Materials* 355.1 (2006), pp. 10–20. DOI: <https://doi.org/10.1016/j.jnucmat.2006.03.015>.
- [34] K. A. Terrani, N. A. Capps, M. J. Kerr, C. A. Back, A. T. Nelson, B. D. Wirth, S. L. Hayes and C. R. Stanek. ‘Accelerating nuclear fuel development and qualification: Modeling and simulation integrated with separate-effects testing’. In: *Journal of Nuclear Materials* 539 (2020), p. 152267. DOI: <https://doi.org/10.1016/j.jnucmat.2020.152267>.

- [35] J. Thomas, A. Figueroa Bengoa, S. T. Nori, R. Ren, P. Kenesei, J. Almer, J. Hunter, J. Harp and M. A. Okuniewski. ‘The application of synchrotron micro-computed tomography to characterize the three-dimensional microstructure in irradiated nuclear fuel’. In: *Journal of Nuclear Materials* 537 (2020), p. 152161. DOI: <https://doi.org/10.1016/j.jnucmat.2020.152161>.
- [36] B. H. Toby and R. B. Von Dreele. ‘GSAS-II: the genesis of a modern open-source all purpose crystallography software package’. In: *Journal of Applied Crystallography* 46.2 (Apr. 2013), pp. 544–549. DOI: [10.1107/S0021889813003531](https://doi.org/10.1107/S0021889813003531).
- [37] J. Turner, J. Buckley, R. Worth, M. Salata-Barnett, M. Schmidt and T. Abram. ‘UN-UB2 Composite fuel material; improved water tolerance with integral burnable absorber’. In: *Journal of Nuclear Materials* 559 (2022), p. 153471. DOI: <https://doi.org/10.1016/j.jnucmat.2021.153471>.
- [38] J. Turner, F. Martini, J. Buckley, G. Phillips, S. Middleburgh and T. Abram. ‘Synthesis of candidate advanced technology fuel: Uranium diboride (UB<sub>2</sub>) via carbo/borothermic reduction of UO<sub>2</sub>’. In: *Journal of Nuclear Materials* 540 (2020), p. 152388. DOI: <https://doi.org/10.1016/j.jnucmat.2020.152388>.
- [39] J. Turner and T. Abram. ‘Steam performance of UB<sub>2</sub>/U<sub>3</sub>Si<sub>2</sub> composite fuel pellets, compared to U<sub>3</sub>Si<sub>2</sub> reference behaviour’. In: *Journal of Nuclear Materials* 529 (2020), p. 151919. DOI: <https://doi.org/10.1016/j.jnucmat.2019.151919>.
- [40] J. K. Watkins, A. R. Wagner, A. Gonzales, B. J. Jaques and E. S. Sooby. ‘Challenges and opportunities to alloyed and composite fuel architectures to mitigate high uranium density fuel oxidation: Uranium diboride and uranium carbide’. In: *Journal of Nuclear Materials* 560 (2022), p. 153502. DOI: <https://doi.org/10.1016/j.jnucmat.2021.153502>.
- [41] A. Zalkin and D. H. Templeton. ‘The crystal structures of CeB<sub>4</sub> ThB<sub>4</sub> and UB<sub>4</sub>’. In: *Acta Crystallographica* 6.3 (Mar. 1953), pp. 269–272. DOI: [10.1107/S0365110X53000764](https://doi.org/10.1107/S0365110X53000764).
- [42] S. Zalkind, G. Rafailov, I. Halevy, T. Livneh, A. Rubin, H. Maimon and D. Schweke. ‘Uranium oxidation kinetics monitored by in-situ X-ray diffraction’. In: *Journal of Nuclear Materials* 485 (2017), pp. 202–206. DOI: <https://doi.org/10.1016/j.jnucmat.2016.12.021>.